

PAPER

Phase transition between pure modes A and B in a circular cylinder's wake. Part I: analysis of fluid forces

To cite this article: L M Lin 2023 *Fluid Dyn. Res.* **55** 035502

View the [article online](#) for updates and enhancements.

You may also like

- [The passive control of three-dimensional flow over a square cylinder by a vertical plate at a moderate Reynolds number](#)
S Malekzadeh, I Mirzaee, N Pourmahmoud et al.
- [Spanwise phase transition between pure modes A and B in a circular cylinder's wake. Part II: spatiotemporal evolution of vorticity](#)
L M Lin
- [Initially generated pure mode A in the three-dimensional wake transition of a circular cylinder](#)
L M Lin

Phase transition between pure modes A and B in a circular cylinder's wake. Part I: analysis of fluid forces

L M Lin 

Key Laboratory for Mechanics in Fluid Solid Coupling Systems, Institute of Mechanics, Chinese Academy of Sciences, Beijing 100190, People's Republic of China

E-mail: llmbirthday@163.com

Received 22 December 2022; revised 2 March 2023

Accepted for publication 25 April 2023

Published 9 May 2023

Communicated by Professor Hyung Jin Sung



CrossMark

Abstract

Through direct numerical simulations, the transition from pure mode A to mode B in the near wake of a circular cylinder is studied with no effect of vortex dislocations. The Reynolds number is computed from 100 to 330 with the computational spanwise length of 4 diameters. In the present part, fluid forces are analyzed. The results show that mode swapping still exists in the range of Reynolds numbers from 230 to 240. In this range, fluid forces with low and high levels occur intermittently. Moreover, when the critical Reynolds number of 193 (± 0.5) is exceeded, with the increase of the Reynolds number, the vortex-shedding frequency gradually shifts from a single low frequency, high and low frequency coexistence to a single high frequency.

Keywords: phase transition, wake, circular cylinder, mode A, mode B

1. Introduction

A bluff body is widely used in many engineering applications, such as suspension bridges, high architectures, flexible risers and heat exchangers. Flow past a bluff body is a classical and basic subject in fluid mechanics. One main reason is the appearance of unsteady wake associated with vortices alternately shedding behind a body. Resultantly, the large unsteady fluid forces are acted on a body, which has the potential to cause the fatigue damage and even destroy the structural integrity. With the aim of understanding and controlling the wake vortex dynamics, a large number of studies (Karniadakis and Triantafyllou 1992, Wu and Ling 1993, Barkley and

Henderson 1996, Williamson 1996a, 1996b, Henderson 1997, Prasad and Williamson 1997, Leweke and Williamson 1998, Persillon and Braza 1998, Ling and Chang 1999, Barkley *et al* 2000, Darekar and Sherwin 2001, Posdziech and Grundmann 2001, Thompson *et al* 2001, Sheard *et al* 2003, Rao *et al* 2013, Jiang *et al* 2016, 2017, 2018, Agbaglah and Mavriplis 2017, 2019, Jiang and Cheng 2019) have been published in recently several decades by applying many methods, including physical model testing, direct numerical simulations (DNSs), and linear or non-linear stability analysis. Comprehensive reviews can be found in previous references (Williamson 1996a, Posdziech and Grundmann 2001).

As a typical example, in a flow past a circular cylinder, four laminar stages for different flow structures in the wake mainly appear in a wake transition sequence (Williamson 1996a). In the laminar steady regime at a Reynolds number Re below around 49, where Re is defined based on the approaching flow velocity U_∞ , the cylinder diameter D and the kinematic viscosity ν of the fluid, the wake comprises a steady recirculation region of two symmetrically placed vortices on each side of the wake. After the primary wake instability is emerged at $Re > 49$ due to a Hopf bifurcation, the two-dimensional (2D) spanwise vortices (with spanwise vorticity ω_z) are alternately shed from the body, known as Kármán vortex streets, in the laminar vortex shedding regime at $Re < 140 \sim 194$. Until Re reaches about 260, two discontinuous changes, mainly associated with two wake instabilities, i.e. modes A and B, in the wake formation appear in the 3D (3D) laminar wake transition regime. Beyond a Reynolds number of 260 in the last stage, a particularly ordered 3D streamwise vortex structure (with streamwise vorticity ω_x) in the near wake, the fine-scale three dimensionality, becomes increasingly disordered, while the primary wake instability behaves remarkably like the laminar shedding mode.

In particular, in the 3D laminar wake-transition regime, two different wake instabilities, typically manifested by the variation of Strouhal number St (non-dimensional vortex-shedding frequency) as Re increases, appear successively with their specific mechanisms and features (Williamson 1996a, Leweke and Williamson 1998, Ling and Chang 1999, Thompson *et al* 2001, Jiang *et al* 2016). At the first discontinuity which is hysteretic near $Re = 180 \sim 194$, the first wake instability, i.e. (pure) mode A, occurs with the inception of vortex loops due to the spanwise wavy deformation of primary vortices as they are shed. Such deformation is caused by an elliptic instability of the primary vortex cores and the formation of streamwise vortex pairs at a spanwise wavelength of around $3 \sim 4$ diameters are resulted from Biot-Savart induction. At the second discontinuous change in the $St - Re$ relation over a range of Re from 230 to 250, the second wake instability, i.e. (pure) mode B, gradually appears due to a gradual transfer of energy from mode A shedding. Such mode B comprises finer-scale streamwise vortices, with a spanwise length scale of around one diameter. It is mainly due to a hyperbolic instability of the braid shear layer region. In addition, there are other formation mechanisms (Yokoi and Kamemoto 1992, 1993, Brede *et al* 1996, Agbaglah and Mavriplis 2017, Lin *et al* 2019, Lin and Tan 2019, 2022, Kokash and Agbaglah 2022), such as vortex tongues under an instability of the braid region (Brede *et al* 1996), an axial stretching of the upstream perturbed vorticity (Agbaglah and Mavriplis 2017) and the 3D instability on and near the cylinder surface coupling with the vortex-induced vortex mechanism (Lin *et al* 2019, Lin and Tan 2019, Lin 2022) in mode A.

Except above two pure modes, there is a large intermittent low-frequency wake velocity fluctuation owing to the presence of large-scale spot-like vortex dislocations in the wake transition with mode A, i.e. mode A* (mode A + vortex dislocations) (Williamson 1996a). The critical Reynolds number Re_{cr} at which mode A* wake instability emerges is identified at 194 through careful experiments, in which the end effects are eliminated by using non-mechanical end conditions (Williamson 1996b). This value is very close to those of $188.5 (\pm 1.0)$, 190

(± 0.02) and 190.5 predicted through linear stability analysis (Barkley and Henderson 1996, Posdziech and Grundmann 2001, Rao *et al* 2013), and 194 and 195 (at most) calculated by DNS (Jiang *et al* 2016, Lin 2022). Besides, the effect of mode A* instability would destabilize mode B in the nonlinear interaction between the two modes (Henderson 1997). This leads to the first emergence of mode B instability at $Re \sim 230$ in experiments (Williamson 1996b) much lower than the critical Re of 259 and 261 (± 0.2) predicted through linear stability analysis (Barkley and Henderson 1996, Posdziech and Grundmann 2001), but in good agreement with predicted $Re = 230$ based on nonlinear stability analysis (Barkley *et al* 2000, Sheard *et al* 2003). Moreover, the experimental study has revealed that the wake transition from mode A* to mode B is a gradual process with intermittent swapping between the two modes (Williamson 1996b). Therefore, the appearance of mode A* or vortex dislocations will seriously interfere both pure modes A and B in the 3D wake transition of a circular cylinder.

Correspondingly, a curious question arises: whether vortex dislocations are an indispensable condition in the transition from mode A to mode B. In other words, when the phenomenon of vortex dislocations is missing, such mode transition should be a simple process, i.e. no mode swapping, or still a gradual progress with intermittent swapping.

In the present work, the primary aim is to explore the possible transition from pure mode A to mode B without any interference of vortex dislocations based on DNS. Therefore, only one spanwise wavelength of four diameters is taken into account, near the most unstable wavelength (Williamson 1996a, Henderson 1997). As the first part of this study, the fluid forces are analyzed. The rest of this paper is organized in the following manner. The governing equations coupled boundary conditions and numerical methods are firstly presented. Then, time histories of fluid forces and frequency analysis are mainly investigated and discussed in detail. Finally, conclusions are obtained.

2. Numerical simulations

As shown in figure 1(a), the fluid flow past a fixed cylinder with a circular cross-section is studied. The fluid is incompressible with constant density ρ and kinematic viscosity ν . All body forces are conservative and then can be reduced to a part of pressure.

The inertial Cartesian coordinate system, (x, y, z) , is established as shown in figure 1(a). Among the axes, the x -axis (streamwise direction) is aligned to the incoming free stream with uniform velocity U_∞ . The z -axis (spanwise direction) is parallel to the cylinder span. The y -axis (vertical direction) is transverse to both the free stream and the cylinder axis.

The incompressible continuity and Navier–Stokes equations in dimensionless forms are written as:

$$\nabla \cdot \mathbf{u} = 0, \quad (2.1)$$

$$\frac{\partial \mathbf{u}}{\partial t} + (\mathbf{u} \cdot \nabla) \mathbf{u} = -\nabla p + \frac{1}{Re} \nabla^2 \mathbf{u}, \quad (2.2)$$

where ∇ is the gradient operator, \mathbf{u} is the velocity vector with three components (u, v, w) along its own coordinate, t is the time scaled by D/U_∞ , p is the pressure scaled by ρU_∞^2 , and Re is the Reynolds number defined by $U_\infty D/\nu$. The velocities are scaled by the free-stream velocity U_∞ and the lengths by the cylinder diameter D . Thus, all variables used in the following context are scaled by ρ , U_∞ and D .

In the present study, some main variables and parameters are involved. The vorticity $\boldsymbol{\omega}$ is defined as the curl of velocity \mathbf{u} , i.e. $\boldsymbol{\omega} = \nabla \times \mathbf{u}$, with three components $(\omega_x, \omega_y, \omega_z)$ along

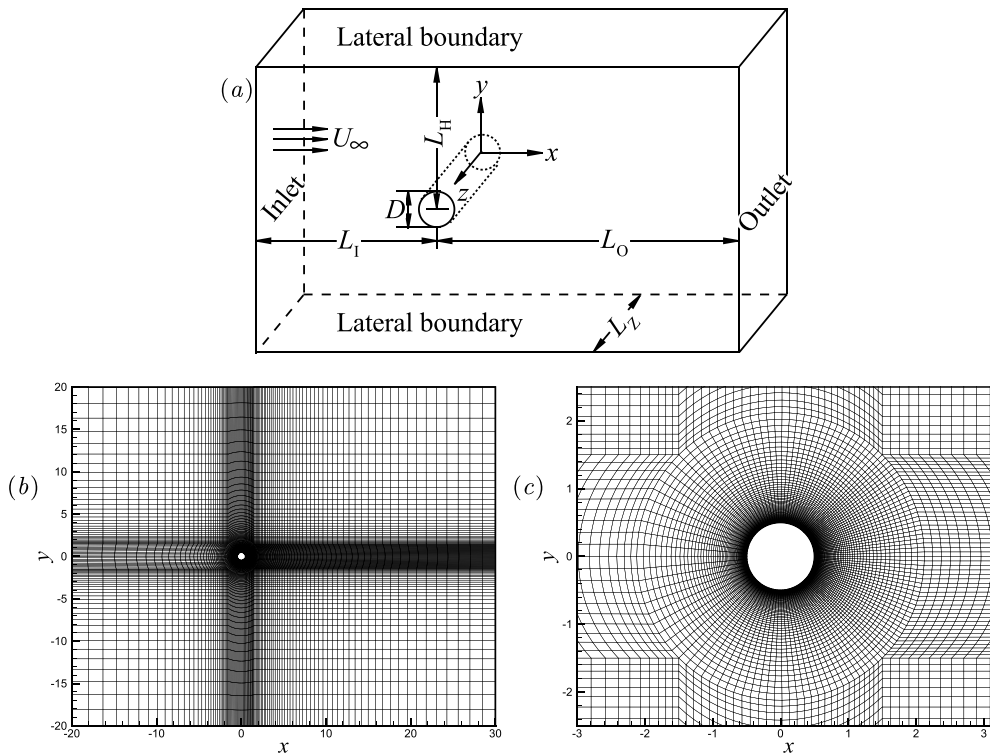


Figure 1. (a) Schematics of a flow past a straight cylinder with a circular cross-section, and computational domain in the (x, y) plane and mesh distributions in (b) the whole flow region and (c) near the cylinder with a closer view.

its coordinate. As an important indicator in the present fluid dynamics, variations in the drag and lift forces acting on the body are taken into account and normalized as the drag and lift coefficients, C_D and C_L , respectively. Then, the mean drag coefficient, \bar{C}_D , and the root-mean-square (RMS) lift coefficient, C'_L , are used to determine the intensity of fluid forces. When spanwise vortices are alternately shed in the near wake, the frequency of such shedding vortex, f , is obtained through Fourier analysis of the time history of C_L . It is scaled as the Strouhal number, St , defined by $St = fD/U_\infty$.

As for the initial condition, the flow is assumed to be motionless with $\mathbf{u} = 0$ and $p = 0$ at $t = 0$, except at the inlet.

As for the boundary conditions, as shown in figure 1(a), the 3D flow is first assumed to be spatially periodic across the span. At the inlet, the uniform free stream is prescribed as $u = U_\infty$ and $v = w = 0$. At the outlet, the simple outflow with $\partial u / \partial x = 0$ is applied. At both lateral boundaries along the $\pm y$ -axis, the free-slip boundary condition with $\frac{\partial u}{\partial y} = v = \frac{\partial w}{\partial y} = 0$ is adopted. On the cylinder surfaces, the no-slip boundary condition with $\mathbf{u} = 0$ is used. The reference pressure of $p_\infty = 0$ is specified at the center of the inlet.

As shown in figure 1(a), the whole nondimensional computational domain for the present wake flow is mainly described by the inlet length $L_I = 20$, the outlet length $L_O = 30$, the vertical height $L_H = 20$ and the computational spanwise length or cylinder span $L_Z = 4$. Therefore, the 3D computational domain, $(L_I + L_O) \times (2L_H) \times L_Z$, is $(20 + 30) \times 40 \times 4$, mainly

Table 1. Summary of hydrodynamic parameters, \bar{C}_D , C'_L and St , in 2D and 3D calculations at $Re = 193$ with $L_Z = 4$. Note that the numbers in parentheses represent the relative errors from the basic case $0^\#$ in 3D numerical simulations.

Cases	N_{xy}	Δz	\bar{C}_D (%)	C'_L (%)	St (%)
2D	20 100	—	1.3318	0.4562	0.1934
3D: $0^\#$	20 100	0.10	1.2597 (0.0)	0.3558 (0.0)	0.1801 (0.0)
3D: $1^\#$	35 400	0.10	1.2541 (0.4)	0.3487 (2.0)	0.1793 (0.4)
3D: $2^\#$	20 100	0.05	1.2605 (0.1)	0.3566 (0.2)	0.1801 (0.0)

used in present simulations. The blockage ratio β , defined by $1/(2L_H)$, is then 2.5%. In addition, $L_Z = 1$ and 2 are also computed in the appearance of mode B.

The mesh distribution in the 2D computational domain is presented in figure 1(b). The smallest grid size of 0.001 is the normal distance of the first layer of the mesh next to the cylinder surface. A local mesh is mainly refined in the large circular region with a diameter approximately 4.24, as shown in figure 1(c). A coarse mesh is mainly distributed far from the cylinder. The total element number of the present 2D mesh N_{xy} is 20 100. As already analyzed and reported in previous works (Henderson 1997, Lin and Tan 2019), a uniform spanwise grid size, $\Delta z = 0.1$, is estimated and adopted.

The dimensionless time step Δt is 0.01. Here, the maximal cell Courant number, $Co = |u|\Delta t/\Delta l$, is less than approximately 0.8, where Δl is the cell size in the direction of the local velocity u through a cell.

Numerical calculations are performed by using FLUENT V6.3.26 software with the finite-volume method. The viscous model adopts the ‘Laminar’. The pressure-implicit splitting of operators algorithm as a pressure-velocity coupling scheme is applied. For the discretization scheme, the second order is applied for the pressure equation; the second-order upwind scheme is used in solving the momentum equation; and the second-order implicit scheme is adopted in all unsteady formulations. In particular, the gradient computation is solved by the Green-Gauss node-based method.

The dimensionless error of the mass conservative equation, equation (2.1), reaches the maximal order of magnitude of $O(10^{-7})$, while the nondimensional errors of three components of the momentum equation, equation (2.2), are lower with the order of $O(10^{-9})$.

The numerical model used here and independence studies about the computational domain and mesh distributions have been already carried out in detail and can refer to previous studies (Lin and Tan 2019, 2022, Lin 2022) because of completely same computational domain and mesh distributions. Particularly, at the critical Reynolds number of 193, a mesh sensitivity analysis is performed, as shown in table 1 with relative errors less than 2%.

3. Results and discussion

3.1. Time histories of fluid forces

Here, only time histories of fluid forces with the computational spanwise length of 4 are presented and discussed, as shown in figures 2 and 3, at different Reynolds numbers. When the Reynolds number is less than 210, as shown in figures 2(a) and (b), fluid forces oscillate with constant amplitudes. When the Reynolds number increases near 210, the peak-to-peak amplitudes of fluid forces obviously appear to vary slightly with time, as shown in figure 2(c). The maximal oscillating amplitude of the lift coefficient, $A_{C_{L,max}}$, is about 0.5. Subsequently, as the Reynolds

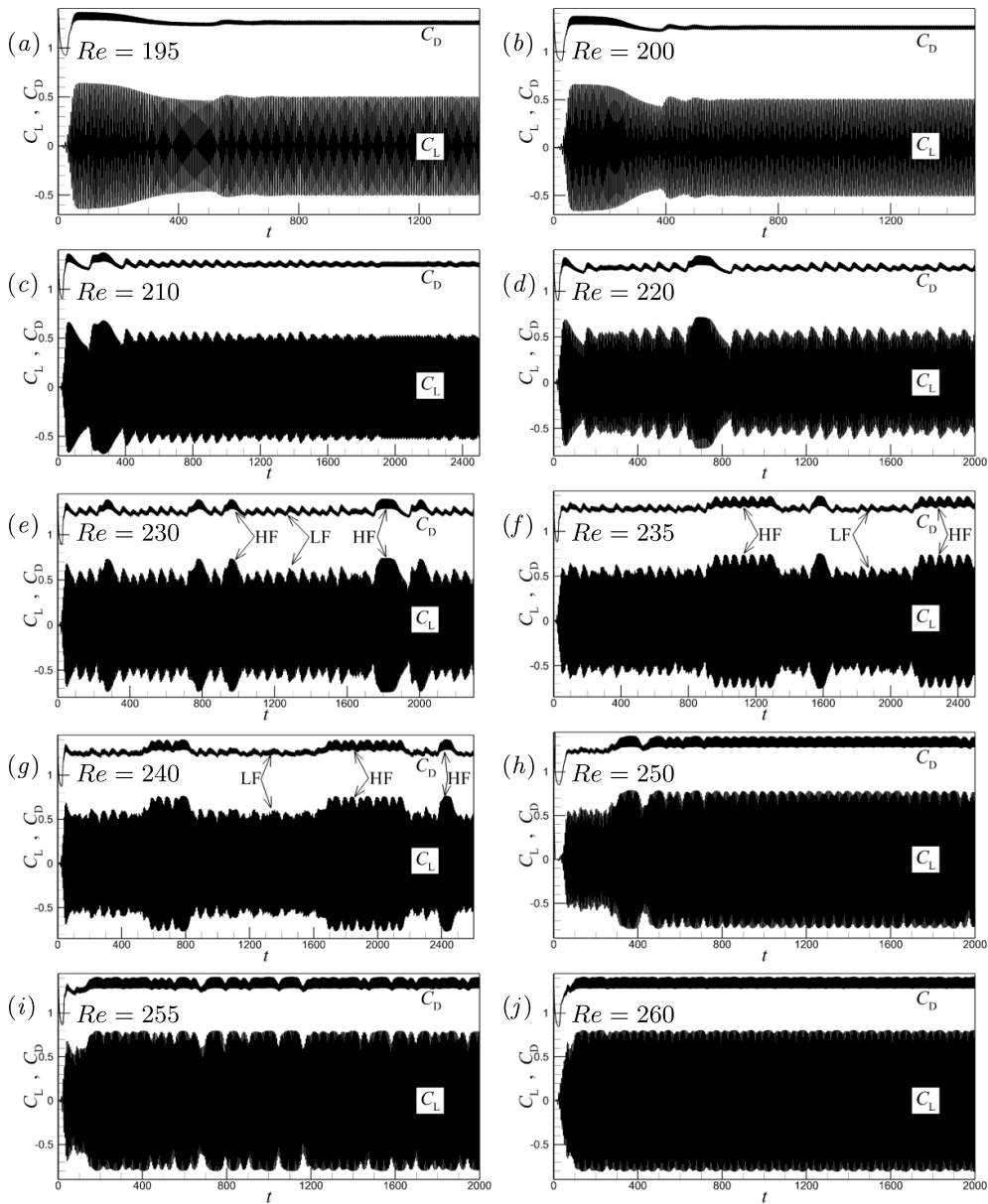


Figure 2. Time histories of force coefficients when $L_Z = 4$ at $Re \in [195, 260]$, where HF and LF in sub-figures (e)–(g) denote oscillating fluid forces at high and low levels, respectively.

number further increases within a range from 220 to 240, as shown in figures 2(d)–(g), fluid forces with oscillating amplitudes at a high level (e.g. $A_{C_L \max} \sim 0.7$) and a low level (same as those with $A_{C_L \max} \sim 0.5$), denoted by ‘HF’ (high force) and ‘LF’ (low force), respectively, appear intermittently and alternately. When the Reynolds number reaches up to 250, fluid forces with oscillating amplitudes at a low level totally disappear, as shown in figure 2(h).

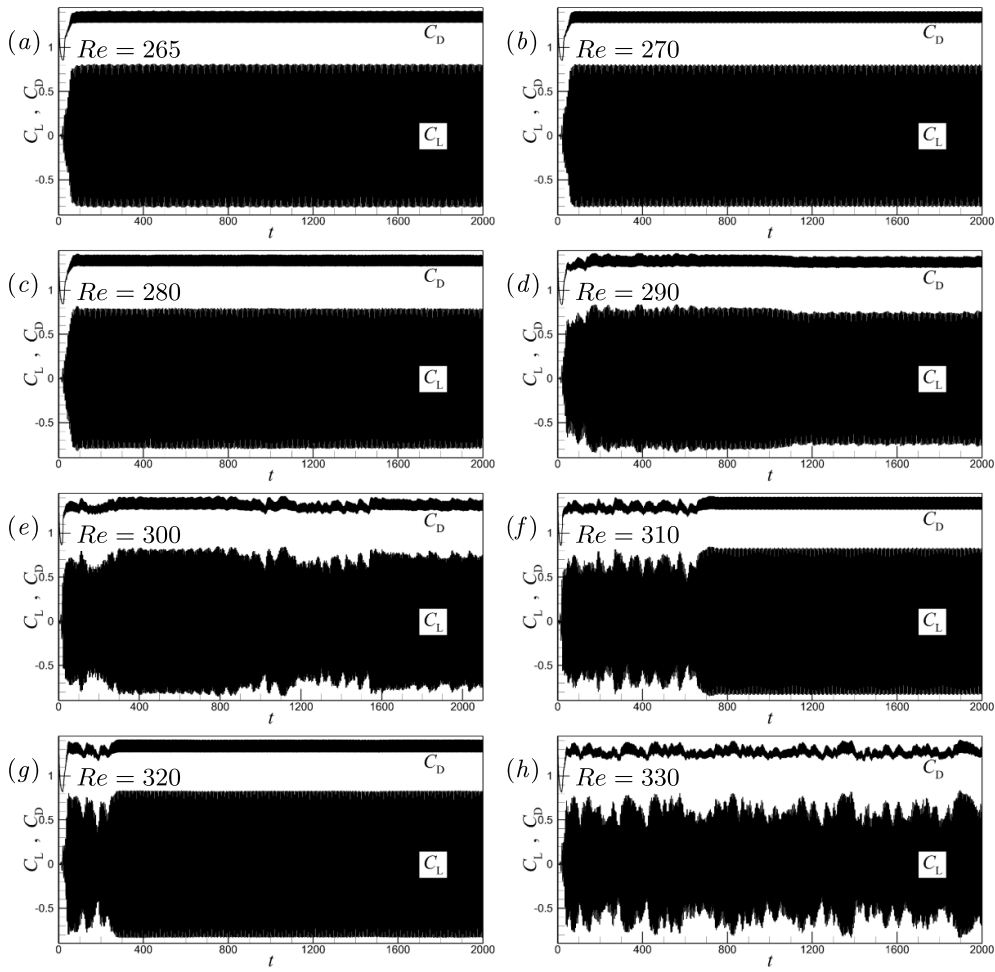


Figure 3. Time histories of force coefficients when $L_Z = 4$ at $Re \in [265, 330]$.

Finally, only oscillating fluid forces at a high level, e.g. $A_{C_L, \max} \sim 0.8$, exist and are almost invariant with time until the Reynolds number is 320, as shown in figures 2 and 3.

3.2. Mean drag and RMS lift forces

Figure 4 presents the mean drag coefficient ($\overline{C_D}$) and RMS lift coefficient (C'_L) versus the Reynolds number, including computations with $L_Z = 1, 2, 4$ and 12 at the specific Reynolds number range. As for computational results with $L_Z = 4$, when the Reynolds number is less than 193, the mean drag coefficient and RMS lift coefficient are almost equivalent to those in 2D computations. Once the Reynolds number exceeds 193, $\overline{C_D}$ and C'_L suddenly drop to a low level, such as, $\overline{C_D} \sim 1.26$ and $C'_L \sim 0.35$. Therefore, the critical Reynolds number at which the pure mode A is fully developed is $193 (\pm 0.5)$ with the Re interval of 1. Then, the mean drag coefficient gradually decreases while the RMS lift coefficient increases until Reynolds number is 240. Because of a gradual appearance of fluid forces at a high level as $Re \geq 230$, the mean drag coefficient and RMS lift coefficient at this high level all quickly increase and approach the

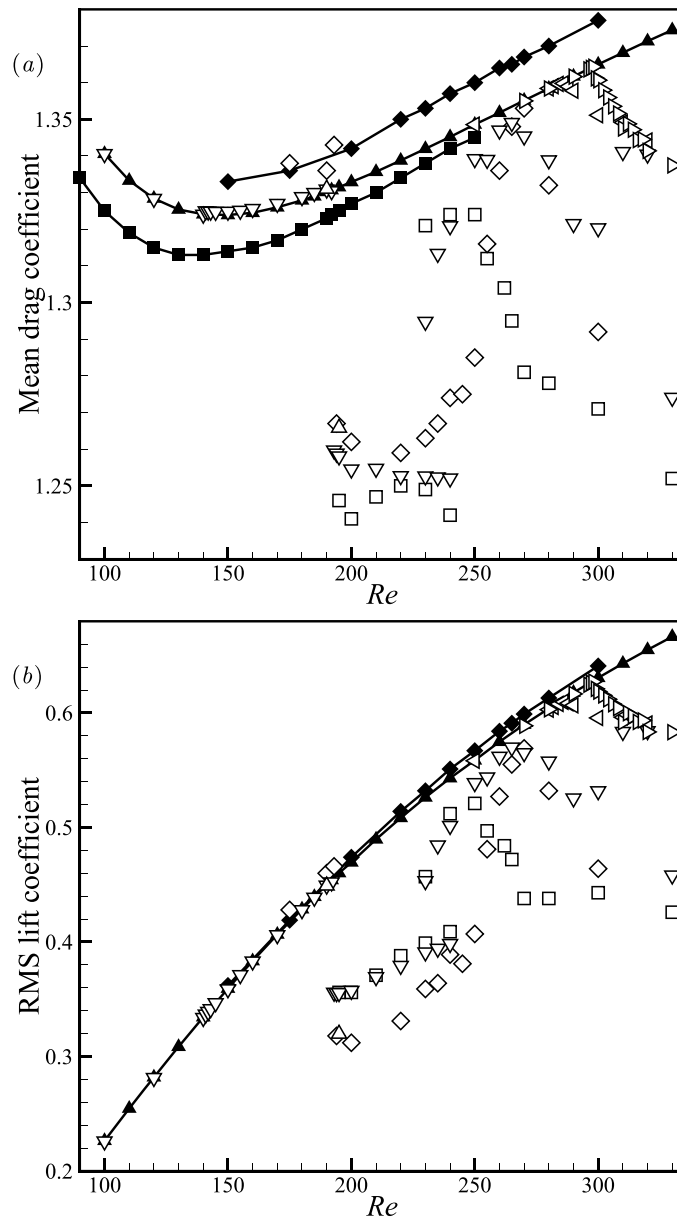


Figure 4. (a) Mean drag coefficient, \bar{C}_D , and (b) RMS lift coefficient, C'_L , versus Re . Data: ■, Posdziech & Grundmann (2001, 2D Num.); □, Posdziech & Grundmann (2001, 3D Num. with $L_Z = 3.746$); ◆, Jiang *et al* (2016, 2D Num.); ◇, Jiang *et al* (2016, 3D Num. with $L_Z = 12$); ▲, Lin (2022, 2D Num.); △, Lin (2022, 3D Num. with $L_Z = 12$ at $Re = 190$ and 195); ▽, present (3D Num. with $L_Z = 4$ at $Re \in [100, 330]$); ◁, present (3D Num. with $L_Z = 2$ at $Re \in [250, 320]$); ▷, present (3D Num. with $L_Z = 1$ at $Re \in [270, 330]$).

2D calculations as the Reynolds number increases to 265. Subsequently, they decrease again until the Reynolds number is about 300. In the range of Reynolds numbers from 310 to 320, the present \bar{C}_D and C'_L suddenly increase and are all close to those with $L_Z = 1$ and 2.

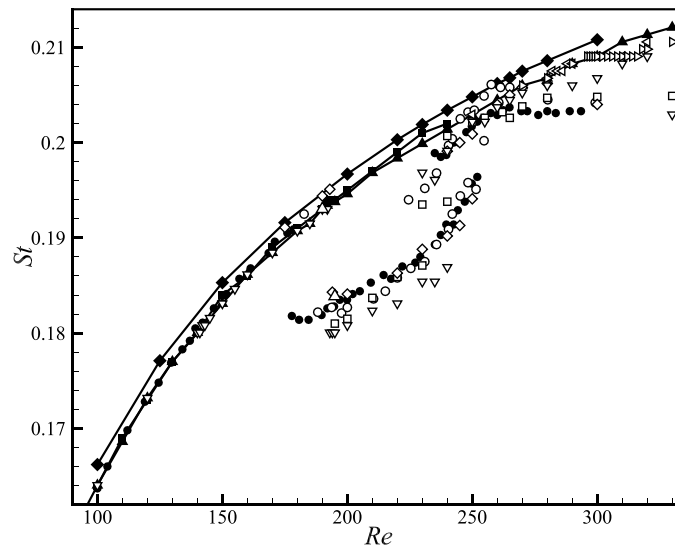


Figure 5. $St - Re$ relationship. Data: ●, Williamson (1996, Exp.); ○, Prasad & Williamson (1997, Exp.); ■, Posdziech & Grundmann (2001, 2D Num.); □, Posdziech & Grundmann (2001, 3D Num. with $L_Z = 3.746$); ◆, Jiang *et al* (2016, 2D Num.); ◇, Jiang *et al* (2016, 3D Num. with $L_Z = 12$); ▲, Lin (2022, 2D Num.); △, Lin (2022, 3D Num. with $L_Z = 12$ at $Re = 190$ and 195); ▽, present (3D Num. with $L_Z = 4$ at $Re \in [100, 330]$); ◁, present (3D Num. with $L_Z = 2$ at $Re \in [250, 320]$); ▷, present (3D Num. with $L_Z = 1$ at $Re \in [270, 330]$).

3.3. Analysis of vortex-shedding frequency

As for the vortex-shedding frequency obtained by Fourier analysis of the lift coefficient $C_L(t)$, $St - Re$ relationship and power spectral density in frequency analysis at different Reynolds numbers are presented in figures 5 and 6, respectively. The frequency resolution is 7.6×10^{-4} and the time interval of the wavelet analysis is the last 1000 to 1300. Similar to fluid forces versus the Reynolds number, as the Reynolds number increases up to 193, St gradually increases at first and is equivalent to that in 2D computations. When $Re \in [193, 240]$, St suddenly drops and then gradually increases, associated with fluid forces at a low level, as shown in figures 7 and 8 through Morlet wavelet analysis. Corresponding to the initial appearance of fluid forces at a high level at $Re \geq 230$, St suddenly jumps to a high value and increases close to that of 2D vortex shedding until Re reaches up to 320. In the range of Reynolds number from 230 to 240, there are two distinct frequencies coexisting in frequency analysis, f_0 and f_1 , as shown in figure 6. These two frequencies, f_0 and f_1 , correspond to fluid forces at a low level and a high level, respectively, also further confirmed by Morlet wavelet analysis as shown in figures 7 and 8, that is LF with f_0 and HF with f_1 . The frequency difference, $f_1 - f_0$, is almost constant, approximately 0.012. Out of this range, only one vortex-shedding frequency is detected in present 3D computations with $L_Z = 4$.

In addition, two aspects should be noticed. When $Re \geq 265$ with $L_Z = 4$, or 286 with $L_Z = 2$ or 299 with $L_Z = 1$, the appearance of pure mode B in the near wake significantly reduces fluid forces away from those in 2D computations, but almost has no effect on vortex-shedding frequency, as shown in figures 4 and 5, whenever L_Z is 1, 2 or 4. Meanwhile, in the transition from pure mode A to mode B, the emergence of coexisting fluid forces at low and high levels, as

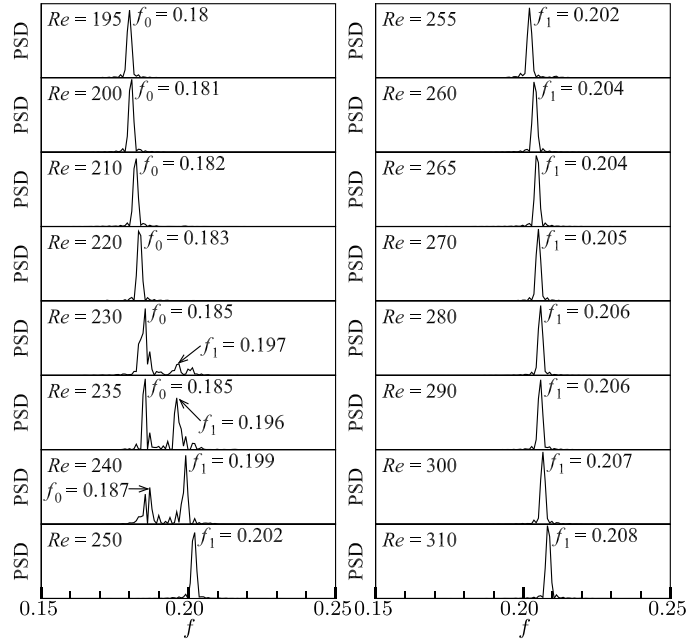


Figure 6. Frequency analysis of $C_L(t)$ at different Reynolds numbers when $L_Z = 4$.

well as two vortex-shedding frequencies, in a certain Re range is independent of the occurrence of vortex dislocations in the near wake.

3.4. Identification of pure modes A and B at $Re \in [230, 240]$

Here, let us identify the appearance of pure modes A and B at the specific Reynolds number range, i.e. $Re \in [230, 240]$, based on special distribution of vorticity signs (Lin *et al* 2018, Lin and Tan 2019, 2022). First, the sign function of the nonzero vorticity ω is defined as $\text{sgn}(\omega) = +1$ when $\omega > 0$ and -1 when $\omega < 0$. Then, at the same spanwise position, the sign relationship, $\text{sgn}(\omega_x)(y > 0) = -\text{sgn}(\omega_x)(y < 0)$ and $\text{sgn}(\omega_y)(y > 0) = \text{sgn}(\omega_y)(y < 0)$, occurs in pure mode A, while the sign relationship, $\text{sgn}(\omega_x)(y > 0) = \text{sgn}(\omega_x)(y < 0)$ and $\text{sgn}(\omega_y)(y > 0) = -\text{sgn}(\omega_y)(y < 0)$, appears in pure mode B, where $y > 0$ and $y < 0$ denote the streamwise and vertical vortices originally shedding from the upper and lower shear layers, respectively. Finally, as shown in figures 9–13, isosurfaces of three components of vorticity are presented mainly at $Re = 235$ and 240, taking into account when the fluid forces are at low and high levels, respectively.

When $Re = 235$, at least three vortex-shedding patterns are identified. At low levels of fluid forces, as shown in figure 9, only the pure mode A appears in the near wake. However, at high levels of fluid forces, sometimes pure mode A exists in the near wake, as shown in figure 10, and sometimes a mixed mode of mode A and mode B occurs, as shown in figure 11, where the streamwise vorticity with the spanwise wavelength of $L_Z = 4$ occurs mainly in the shear layer or local region of $x < 6$, while the streamwise vorticity with the spanwise wavelength of approximately $\frac{1}{4}L_Z = 1$ appears mainly in the shedding vortex or region of $x > 6$. Therefore, from this point of view, mode swapping also includes the case in which two modes A and B coexist at different streamwise positions in a certain time interval. Moreover, fluid forces at a

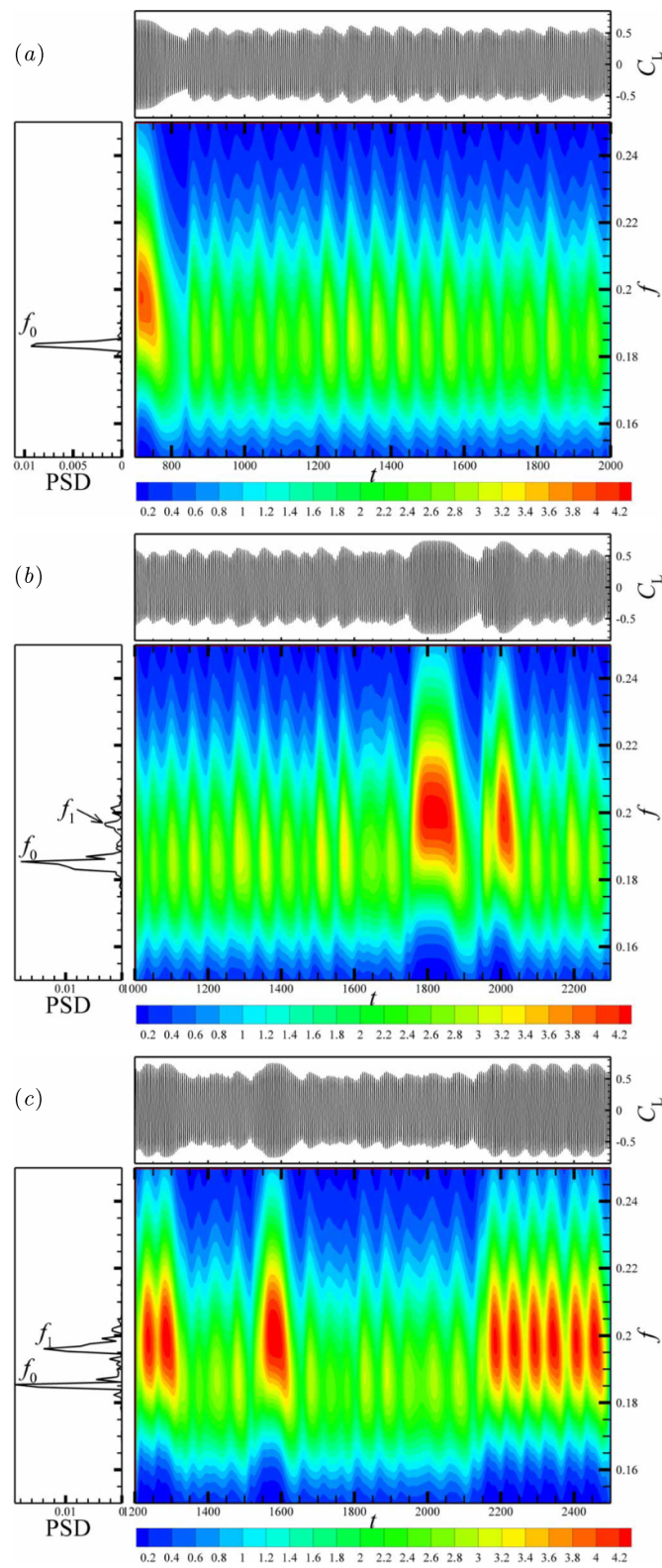


Figure 7. Frequency spectra of C_L^{11} in 3D wakes with $L_Z = 4$ obtained through Morlet wavelet analysis at Reynolds numbers of (a) 220, (b) 230 and (c) 235.

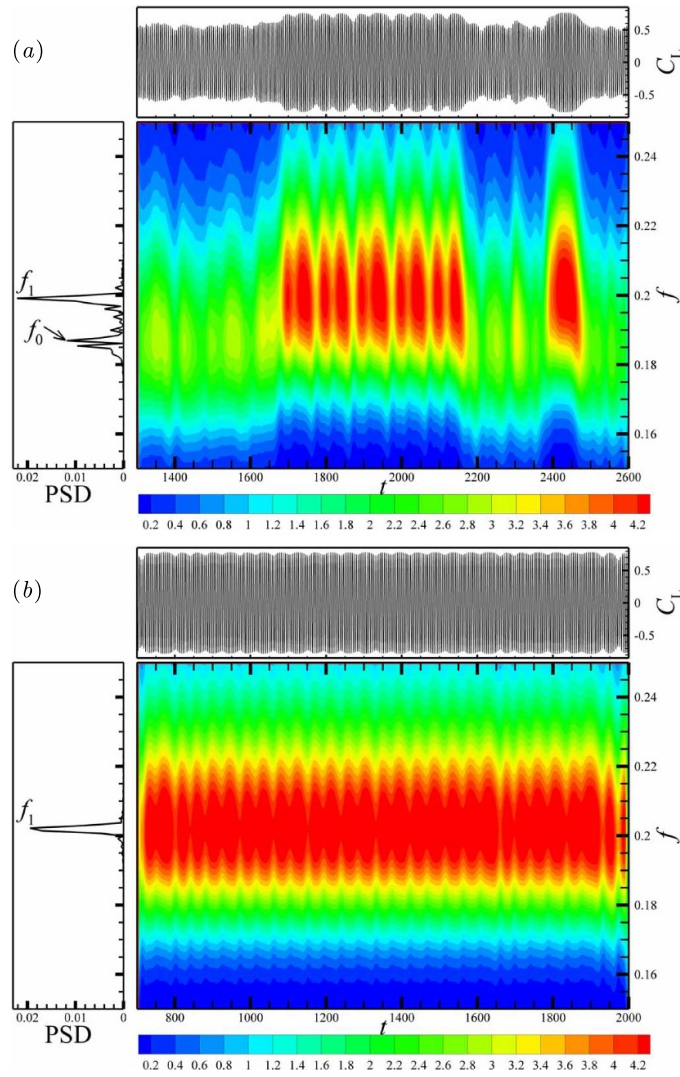


Figure 8. Frequency spectra of C_L in 3D wakes with $L_Z = 4$ obtained through Morlet wavelet analysis at Reynolds numbers of (a) 240 and (b) 250.

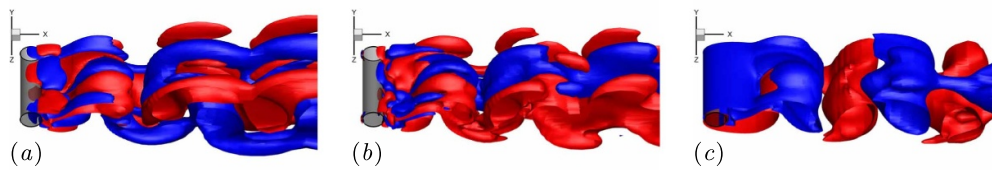


Figure 9. At $t = 1801.5$ (LF), isosurfaces of (a) $\omega_x = \pm 0.1$, (b) $\omega_y = \pm 0.1$ and (c) $\omega_z = \pm 0.2$ in the near wake of a circular cylinder with $L_Z = 4$ at $Re = 235$, where red and blue colors denote positive and negative values, respectively. Note that the cylinder is denoted by the grey translucent surface and the flow is from left to right.

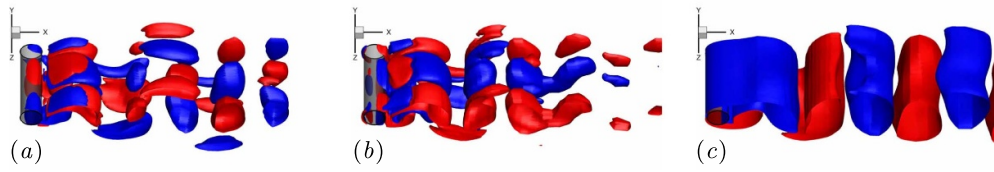


Figure 10. At $t = 2242$ (HF), isosurfaces of (a) $\omega_x = \pm 0.1$, (b) $\omega_y = \pm 0.05$ and (c) $\omega_z = \pm 0.2$ in the near wake of a circular cylinder with $L_Z = 4$ at $\text{Re} = 235$ (same descriptions as in figure 9).

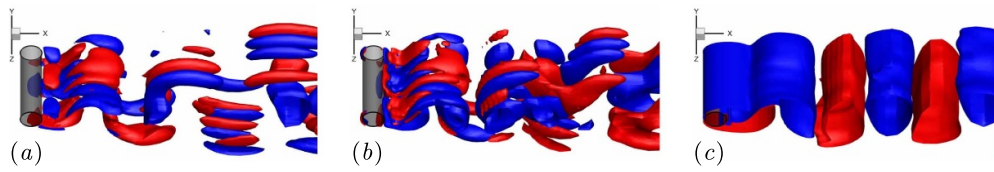


Figure 11. At $t = 2401$ (HF), isosurfaces of (a) $\omega_x = \pm 0.1$, (b) $\omega_y = \pm 0.05$ and (c) $\omega_z = \pm 0.2$ in the near wake of a circular cylinder with $L_Z = 4$ at $\text{Re} = 235$ (same descriptions as in figure 9).

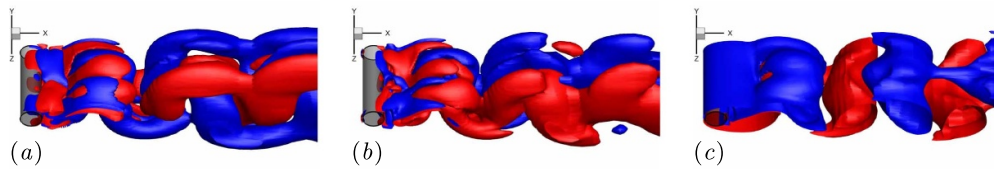


Figure 12. At $t = 2590$ (LF), isosurfaces of (a) $\omega_x = \pm 0.1$, (b) $\omega_y = \pm 0.1$ and (c) $\omega_z = \pm 0.2$ in the near wake of a circular cylinder with $L_Z = 4$ at $\text{Re} = 240$ (same descriptions as in figure 9).

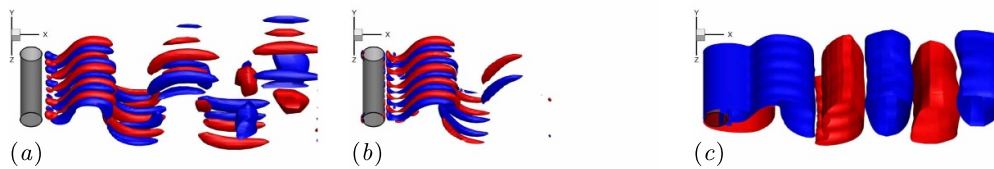


Figure 13. At $t = 2415.5$ (HF), isosurfaces of (a) $\omega_x = \pm 0.1$, (b) $\omega_y = \pm 0.1$ and (c) $\omega_z = \pm 0.2$ in the near wake of a circular cylinder with $L_Z = 4$ at $\text{Re} = 240$ (same descriptions as in figure 9).

high level of do not necessarily correspond to the occurrence of mode B, but sometimes to the emergence of pure mode A.

When $\text{Re} = 240$, at least two vortex-shedding patterns are identified, as shown in figures 12 and 13. Pure modes A and B exist completely independently at two moments with different fluid force levels. Among them, the spanwise wavelength of pure mode B is approximately $\frac{1}{5}L_Z = 0.8$.

In summary, the gradual transition or mode swapping between modes A and B can appear totally irrelevant to the existence of vortex dislocations in the near wake.

4. Conclusions

The phase transition from pure mode A to mode B in the near wake of a circular cylinder is investigated by DNS without any interference of vortex dislocations. The computational spanwise length is 4. The calculated range of the Reynolds number is from 100 to 330. As the first part of this study, the fluid forces are analyzed.

The critical Reynolds number is 193 (± 0.5). Above this critical Reynolds number, fluid forces suddenly decrease due to the fully developed pure mode A. Then, in the Reynolds number range from 230 to 240, there are two levels of fluid forces coexisting in the near wake flow. The frequency analysis shows that fluid forces at a low level have the low vortex-shedding frequency, while those at a high level have the high frequency. Furthermore, the identification of modes A and B, based on special signs of streamwise and vertical vorticities in the near wake, confirms that modes A and B sometimes independently appear, sometimes coexist in the mode swapping at $Re \in [230, 240]$. Therefore, it can be preliminarily judged that the existence of vortex dislocations is not an essential condition in the transition process between modes A and B as the Reynolds number increases.

In the next part of this study, the main focus is put on the spatiotemporal evolution of streamwise and vertical vorticities in the transition from pure mode A to mode B without the effect of vortex dislocations.

Acknowledgments

The authors wish to thank the Hainan Province Science and Technology Special Fund (ZDYF2022GXJS004, ZDYF2021GXJS028) for this work.

Conflict of Interests

The authors report no conflict of interest.

ORCID iD

L M Lin  <https://orcid.org/0000-0001-8933-9630>

References

- Agbaglah G and Mavriplis C 2017 Computational analysis of physical mechanisms at the onset of three-dimensionality in the wake of a square cylinder *J. Fluid Mech.* **833** 631–47
- Agbaglah G and Mavriplis C 2019 Three-dimensional wakes behind cylinders of square and circular cross-section: early and long-time dynamics *J. Fluid Mech.* **870** 419–32
- Barkely D and Henderson R D 1996 Three-dimensional Floquet stability analysis of the wake of a circular cylinder *J. Fluid Mech.* **322** 215–41
- Barkley D, Tuckerman L S and Golubitsky M 2000 Bifurcation theory for three-dimensional flow in the wake of a circular cylinder *Phys. Rev. E* **61** 5247–52
- Brede M, Eckelmann H and Rockwell D 1996 On secondary vortices in the cylinder wake *Phys. Fluids* **8** 2117–24
- Darekar R M and Sherwin S J 2001 Flow past a square-section cylinder with a wavy stagnation face *J. Fluid Mech.* **426** 263–95

- Henderson R D 1997 Nonlinear dynamics and pattern formation in turbulent wake transition *J. Fluid Mech.* **352** 65–112
- Jiang H and Cheng L 2019 Transition to the secondary vortex street in the wake of a circular cylinder *J. Fluid Mech.* **867** 691–722
- Jiang H, Cheng L, Draper S and An H 2017 Prediction of the secondary wake instability of a circular cylinder with direct numerical simulation *Comput. Fluids* **149** 172–80
- Jiang H, Cheng L, Draper S, An H and Tong F 2016 Three-dimensional direct numerical simulation of wake transitions of a circular cylinder *J. Fluid Mech.* **801** 353–91
- Jiang H Y, Cheng L and An H W 2018 Three-dimensional wake transition of a square cylinder *J. Fluid Mech.* **842** 102–27
- Karniadakis G E and Triantafyllou G S 1992 Three-dimensional dynamics and transition to turbulence in the wake of bluff bodies *J. Fluid Mech.* **238** 1–30
- Kokash H and Agbaglah G G 2022 On the origin of mode B instability of the wake of a square cylinder *Phys. Fluids* **34** 074116
- Leweke T and Williamson C H K 1998 Three-dimensional instabilities in wake transition *Eur. J. Mech. B* **17** 571–86
- Lin L M 2022 Initially generated pure mode A in the three-dimensional wake transition of a circular cylinder *Fluid Dyn. Res.* **54** 035504
- Lin L M, Shi S Y and Wu Y X 2018 Intrinsic relationship of vorticity between modes A and B in the wake of a bluff body *Theor. Appl. Mech. Lett.* **8** 320–5
- Lin L M, Shi S Y and Wu Y X 2019 Physical mechanism for origin of streamwise vortices in mode A of a square-section cylinder *Acta Mech. Sin.* **35** 411–8
- Lin L M and Tan Z R 2019 DNS in evolution of vorticity and sign relationship in wake transition of a circular cylinder: (pure) mode A *Acta Mech. Sin.* **35** 1131–49
- Lin L M and Tan Z R 2022 DNS of the spatiotemporal evolution of the vorticity in (pure) mode B of a circular cylinder's wake *Fluid Dyn. Res.* **54** 015511
- Ling G C and Chang Y 1999 Three-dimensional stability analysis of the periodic wake behind a circular cylinder by low-dimensional Galerkin method *Chin. J. Theor. Appl. Mech.* **31** 652–60
- Persillon H and Braza M 1998 Physical analysis of the transition to turbulence in the wake of a circular cylinder by three-dimensional Navier-Stokes simulation *J. Fluid Mech.* **365** 23–88
- Posdziech O and Grundmann R 2001 Numerical simulation of the flow around an infinitely long circular cylinder in the transition regime *Theor. Comput. Fluid Dyn.* **15** 121–41
- Prasad A and Williamson C H K 1997 Three-dimensional effects in turbulent bluff-body wakes *J. Fluid Mech.* **343** 235–65
- Rao A, Thompson M C, Leweke T and Hourigan K 2013 The flow past a circular cylinder translating at different heights above a wall *J. Fluids Struct.* **41** 9–21
- Sheard G J, Thompson M C and Hourigan K 2003 A coupled Landau model describing the Strouhal-Reynolds number profile of a three-dimensional circular cylinder wake *Phys. Fluids* **15** L68–71
- Thompson M C, Leweke T and Williamson C H K 2001 The physical mechanism of transition in bluff body wakes *J. Fluids and Struct.* **15** 607–16
- Williamson C H K 1996a Vortex dynamics in the cylinder wake *Annu. Rev. Fluid Mech.* **28** 477–539
- Williamson C H K 1996b Three-dimensional wake transition *J. Fluid Mech.* **328** 345–407
- Wu Z B and Ling G C 1993 Numerical study on the mechanism for three-dimensional evolution of vortex and the structural features in the wake behind a circular cylinder *Chin. J. Theor. Appl. Mech.* **25** 264–75
- Yokoi Y and Kamemoto K 1992 Initial stage of a three-dimensional vortex structure existing in a two-dimensional boundary layer separation flow (Observation of laminar boundary layer separation over a circular cylinder by flow visualization) *JSME Int. J. II* **35** 189–95
- Yokoi Y and Kamemoto K 1993 Initial stage of a three-dimensional vortex structure existing in a two-dimensional boundary layer separation flow (Visual observation of laminar boundary layer separation over a circular cylinder from the side of a separated region) *JSME Int. J. B* **36** 201–6